A Local Stress Criterion to Assess the Effects of Hydrogen Embrittlement on the Fracture Strength of Notched Tensile Specimens

Claudio Ruggieri[1], Diego Sarzosa[1], and Lenin Paredes Tobar[2]

[1]University of São Paulo
[2]Texas A&M University

February 14, 2023

Abstract

This work addresses the applicability of a local criterion incorporating the coupling of critical stress and a critical hydrogen concentration to predict hydrogen embrittlement effects on the fracture strength of high strength steels using notched round specimens with different notch root radii. The numerical simulations incorporating a relatively simple hydrogen transport model provide strong support to the adoption of a failure criterion in terms of achieving a critical level of tensile stress coupled to the local hydrogen concentration, which, in turn, enable the construction of a failure locus for the material. For the cases analyzed here, construction of such a failure locus based on a critical combination of maximum principal stress and hydrogen concentration enabled predictions of fracture strength for hydrogen-charged tensile specimens which are in very good agreement with experimental data. Overall, the results presented here lend additional support for further developments of a local stress-based criterion to predict hydrogen embrittlement effects on the fracture strength of high strength steels.

A Local Stress Criterion to Assess the Effects of Hydrogen Embrittlement on the Fracture Strength of Notched Tensile Specimens

Claudio Ruggieri[1*], Diego F. B. Sarzosa[1], Marcelo Paredes[2]

February 13, 2023

[1]Department of Naval Architecture and Ocean Engineering, University of São Paulo, São Paulo, Brazil.

[2]Department of Ocean Engineering, Texas A&M University, Texas, USA.

Abstract

This work addresses the applicability of a local criterion incorporating the coupling of critical stress and a critical hydrogen concentration to predict hydrogen embrittlement effects on the fracture strength of high strength steels using notched round specimens with different notch root radii. The numerical simulations incorporating a relatively simple hydrogen transport model provide strong support to the adoption of a failure criterion in terms of achieving a critical level of tensile stress coupled to the local hydrogen concentration, which, in turn, enable the construction of a failure locus for the material. For the cases analyzed here, construction of such a failure locus based on a critical combination of maximum principal stress and hydrogen concentration enabled predictions of fracture strength for hydrogen-charged tensile specimens which are in very good agreement with experimental data. Overall, the results presented here lend additional support for further developments of a local stress-based criterion to predict hydrogen embrittlement effects on the fracture strength of high strength steels.

Keywords: hydrogen embrittlement, notched tensile specimens, finite element analysis, fracture strength, stress criterion

*Corresponding author. Tel.: +55-11-30915184 - Fax: +55-11-30915717 - E-mail address: claudio.ruggieri@usp.br

1 Introduction

Accurate assessments of the mechanical integrity and remaining life of high-strength steel alloy components exposed to a hydrogen environment play a key role in the continued and safe operation of critical engineering structures. Hydrogen-induced fracture is of primary interest here as fast diffusion of H atoms through the solid material followed by interaction with crystal defects promotes severe material degradation at several length scales at the micro and macro levels [1]. This complex process, generally termed hydrogen embrittlement (HE), results in marked reduction of ductility and toughness, particularly for various classes of metallic alloys, including high strength steels, which can lead to catastrophic fast fracture of the engineering component at stresses below its design or operational stress. For example, a number of experimental studies have shown that the fracture toughness of degraded material by HE is reduced by as much as $10 \sim 25\,\%$ of the fracture toughness value for a hydrogen-free material (see, *e.g.*, Gangloff [2] and Ronevich [3] for illustrative data). Consequently, understanding hydrogen-assisted embrittlement in structural materials and, more specifically, high strength is essential to enable safe and reliable operation of critical structural components.

A case of particular interest and major concern involves the potential strong degradation of high strength fasteners for critical marine and subsea applications. As the oil and gas industry is increasingly expanding its exploration and production activities into deep water offshore locations, several of which are hydrocarbon reservoirs having high pressure and high temperature (HPHT) conditions, the subsea equipment must comply with more stringent requirements and specifications for drilling, completing and producing in more hostile environment. Here, bolted connections and fasteners made of high strength steels, mainly AISI 4140 and 4340 steels, and corrosion resistant alloys, such as UNS N07718 [4] (also commercially known as Inconel 718), remain as the primary joint method of high-integrity subsea systems and are, thus, essential for the long-term performance of the subsea infrastructure. However, in marine environments, these components made of high strength materials are highly susceptible to HE associated with hydrogen generated by corrosion reactions or cathodic protection. While recent studies (see the review article of Esaklul and Ahmed [5]) have shown that subsea fasteners exposed to cathodic protection can be safely used provided their hardness is limited to ~ 34 HRC [6, 7, 8], there are still important discrepancies in several industry standards establishing a hardness threshold criterion to avoid hydrogen embrittlement. Fitness-for-service analyses of in-service components under hydrogen embrittlement conditions should employ failure criteria incorporating a more physically-based description of HE micromechanism and which allow relatively simple and conservative assessments most appropriate for engineering-level applications. Perhaps more importantly, with the increased

use of high-strength materials to meet the more stringent demands of HPHT conditions often present in challenging deep-water oil and gas reservoirs [9], development of more effective and realistic approaches addressing the effects of HE on this class of materials remains essential.

Hydrogen embrittlement is arguably one of the most complex phenomena of degradation in metallic materials, causing a hydrogen-induced transition from a high-toughness ductile fracture (micro-void coalescence) to a brittle-type of fracture (either by a transgranular or intergranular mechanism). While there is now a rapidly growing body of research that focuses on the several mechanisms controlling the effects of HE on the mechanical behavior and, more specifically, on the fracture resistance and toughness of steels and metallic alloys (see, *e.g,* the review articles of Barrera et al. [1] and Dadfarnia et al. [10]), a consensus appears to be emerging in favor of two most viable mechanisms: 1) *hydrogen induced decohesion* (HID), also known as *hydrogen-enhanced decohesion* (HEDE), in which hydrogen accumulated at locations of high stress triaxiality, such as ahead of a crack tip, reduces the local cohesive strength and the specific surface energy thereby reducing the fracture toughness [11, 12] and 2) *hydrogen-enhanced localized plasticity* (HELP), in which hydrogen accumulated in a localized region ahead of a crack tip promotes an an increase in dislocation nucleation and mobility thereby increasing plasticity and material softening [13, 14]. While it is now recognized that no single mechanism can comprehensively explain all the phenomena associated with HE at the continuum level, several other hydrogen degradation theories have been proposed incorporating different scales and micromechanisms of HE in steels and metallic alloys [1, 10] - however, these are not germane to the present study.

In this work, we pursue a line of investigation in which the conditions for intergranular fracture instability associated with hydrogen embrittlement in martensitic high strength steels are accounted for in terms of a local criterion incorporating a coupling of critical stress and a critical hydrogen concentration. To the extent that fracture may be expected controlled by the near-tip stress fields, such a criterion makes contact with a hydrogen-induced decohesion type mechanism that describes macroscopic embrittlement in terms of achieving a critical level of tensile stress over a microstructural length-scale physically coupled to the decrease in local cohesive strength caused by hydrogen diffusion. To describe the effects of hydrogen-induced degradation on fracture strength, we employ a computational framework incorporating a material constitutive model that extends a conventional Mises plasticity model to include the effect of diffusible hydrogen on the mechanical (flow) properties. The experimental investigations conducted by Wang et al. [15, 16, 17] provide the quantitative relationship between the tensile strength of notched specimens with varying stress triaxiality and diffusible hydrogen content of a quenched and tempered AISI 4135 steel and a boron-alloyed stees, upon which the influence of hydrogen embrittlement on fracture behavior can

be assessed. Those experimental studies demonstrate that the diffusible hydrogen content plays a key role in reducing the fracture strength of the notched specimens with different levels of stress triaxiality. The adopted computational model then enables defining a failure locus that captures accurately the measured variation of fracture strength with hydrogen content fairly independent of specimen stress triaxiality to produce a viable fracture criterion for hydrogen-degraded engineering components.

The plan of the paper is as follows. To provide some fundamental background and pertinent features of the hydrogen transport model employed in the present work, Section 2 provides a brief description of the kinetics of hydrogen diffusion in metals based on the Oriani theory [18]. In Section 3, we present the essential results derived from the tensile tests performed by Wang et al. [15, 16, 17] on hydrogen charged, high strength steels using notched round specimens with different notch root radii, upon which the proposed local stress criterion to assess effects of hydrogen embrittlement is developed. Numerical procedures and constitutive models are given in Section 4, including a short discussion on the adopted hydrogen-model parameters. Section 5 is concerned with results and discussions, and, more specifically, the applicability of the proposed local stress criterion in terms of a failure locus defining fracture conditions for hydrogen-charged specimens. Concluding remarks follow in Section 6.

2 Kinetics of Hydrogen Diffusion in Metals

This section briefly describes an approximate treatment of a hydrogen transport model that has a direct bearing on the computational framework incorporating the effect of diffusible hydrogen on the mechanical (flow) properties addressed later. The approach presented here draws heavily on previous work of Oriani [18] and Sofronis et al. [19, 20], which considers a local equilibrium of diffusible hydrogen in lattice and trapping sites coupled with local stresses and strains. Readers are referred to these studies and the WARP3D [21] documentation for a more complete discussion of the hydrogen transport model under discussion.

2.1 Hydrogen Diffusion: Oriani Model

Development of a computational model incorporating the effects of hydrogen on the material behavior begins by considering a simplified kinetic model describing the hydrogen diffusion in metals. By assuming that hydrogen resides at either normal interstitial lattice sites (NILS) or at reversible trapping sites, such as microstructural defects generated by plastic deformation [22], and, further, assuming that these two populations are always in equilibrium, Oriani [18]

and Oriani e Josephic [23, 24] proposed a model to describe the local equilibrium of hydrogen in the traps and lattice in terms of

$$\frac{\theta_T}{1-\theta_T} = \frac{\theta_L}{1-\theta_L} \exp\left(\frac{W_B}{RT}\right) \tag{1}$$

where θ_L and θ_T are the occupancies of hydrogen in NILS and trapping sites, W_B represents the trap binding energy, R is the gas constant defined by $8.31\,\mathrm{J\,mol^{-1}\,K^{-1}}$ and T is the absolute temperature in K. The hydrogen concentration per unit volume in trapping sites, C_T, can be written as

$$C_T = \theta_T \alpha N_T \tag{2}$$

where α defines the number of sites per trap and N_T represents the trap density measured in terms of the number of traps per unit volume, which is a function of the local effective plastic strain. Similarly, the hydrogen concentration residing in NILS is expressed by

$$C_L = \theta_L \beta N_L \tag{3}$$

in which β is the number of NILS per solvent atom and N_L defines the number of solvent atoms per unit lattice volume. If the available number of trapping sites per unit volume, αN_T, is smaller than the available NILS per unit volume, βN_L, then

$$N_L = \frac{N_A}{V_M} \tag{4}$$

where $N_A = 6.0232 \times 10^{23}\,\mathrm{atoms/mol}$ is Avogadro's number and V_M defines the molar volume of the host lattice measured in units of volume per lattice mole.

2.2 Hydrogen Concentration in Metals

Further development of a finite element formulation including the effects of hydrogen on the mechanical (flow) properties requires considering the connection between hydrogen transport and the local fields of hydrostatic stress and plastic strain in the material. The hydrogen concentration at NILS, C_L, is assumed to be in equilibrium with local Cauchy stress, σ_{ij}, such that

$$\frac{\theta_L}{1-\theta_L} = \frac{\theta_L^0}{1-\theta_L^0} K_L \tag{5}$$

where $\theta_L^0 = C_L^0/\beta N_L$ is the initial occupancy at NILS and

$$K_L = \exp\left[\frac{\sigma_{kk} V_H}{3RT}\right] \tag{6}$$

is the equilibrium constant determined by the first order interaction between hydrogen-induced lattice dilatation. In the above, the hydrostatic stress is defined as $\sigma_h = \sigma_{kk}/3$ and V_H is the partial molar volume of hydrogen in solution; here, the standard summation convention applies.

Combining Eqs. (4) and (5), and, further, considering that hydrogen trap sites are associated with the effective plastic strain, $\bar{\epsilon}_p$, in the deforming metal, Sofronis et al. [20] arrived at the total hydrogen concentration as

$$C = C_L + C_T = \beta N_L \left[\theta_L \left(\sigma_{kk}\right) + \theta_{TL} \left(\sigma_{kk},\, \bar{\epsilon}_p\right)\right] \tag{7}$$

where

$$\theta_L \left(\sigma_{kk}\right) = \theta_L^0 K_L / \left[\left(1 - \theta_L^0\right) + \theta_L^0 K_L\right] \tag{8}$$

and

$$\theta_{TL} \left(\sigma_{kk},\, \bar{\epsilon}_p\right) = \frac{\alpha N_T \left(\bar{\epsilon}_p\right)}{\beta N_L} \times \frac{K_T \theta_L \left(\sigma_{kk}\right)}{1 - \theta_L \left(\sigma_{kk}\right) + K_T \theta_L \left(\sigma_{kk}\right)} \quad . \tag{9}$$

Given that hydrogen remains in equilibrium with local stresses, Eqs. (7-9) define the total hydrogen concentration based on current values of $\bar{\epsilon}_p$ and σ_{kk}. Alternatively, the total hydrogen concentration can also be expressed in the unit of hydrogen atoms per host metal atom (H/M) as

$$c = C/N_L = \beta \left[\theta_L \left(\sigma_{kk}\right) + \theta_{TL} \left(\sigma_{kk},\, \bar{\epsilon}_p\right)\right] \quad . \tag{10}$$

Moreover, since the effective plastic strain and hydrostatic stress also depend on the amount of hydrogen present in the material, it becomes clear that the problem of determining the hydrogen concentration, local stresses and plastic strains requires a fully coupled solution. Readers are referred to the WARP3D [21] documentation for more detailed information about the above formulations.

3 Hydrogen Embrittlement of Notched Tensile Specimens

Wang et al. [15] conducted tensile tests on a hydrogen charged high strength steel using notched round specimens with different notch root radii. The material is a quenched and tempered, low alloy AISI 4135 steel with yield stress, $\sigma_{ys} = 1235\,\text{MPa}$, and tensile strength, $\sigma_{uts} = 1320\,\text{MPa}$. Figure 1 displays the notched round bar specimens employed in the tensile tests, in which the notch radius, ρ, is 0.1, 0.25 and 0.8 mm. Hydrogen charging of the tensile specimens was performed by an electrochemical method using either an acidic or alkaline aqueous solution at various current densities. Following hydrogen charging of the steel, slow strain rate tensile (SSRT) tests were carried out to determine the dependence of notch

tensile strength on diffusible hydrogen content for the notched specimens. In later related work, Wang et al. [16] also performed tensile tests on a hydrogen charged AISI 4135 steel having a different quenching and tempering treatment and with yield stress, $\sigma_{ys} = 1320\,\text{MPa}$, and tensile strength, $\sigma_{uts} = 1450$ MPa. Here, SSRT tests were also conducted to evaluate the effect of diffusible hydrogen content on the tensile strength for notched specimens with $\rho = 0.1$ and 0.8 mm - these specimens have the same configuration as those already shown in Fig. 1. In the interest of clarity, these materials are hereafter simply referred to as 4135A ($\sigma_{ys} = 1235\,\text{MPa}$) and 4135B ($\sigma_{ys} = 1320\,\text{MPa}$). Additional tensile tests using notched round specimens were also performed by Wang et al. [17] on a quenched and tempered, boron-alloyed steel with yield stress, $\sigma_{ys} = 1160$ MPa, and tensile strength, $\sigma_{uts} = 1305$ MPa. The specimen configuration, hydrogen charging procedure and SSRT tests are essentially similar to those already described previously for the testing program conducted on the AISI 4135 steel. The reader is referred to the works of Wang et al. [15, 16, 17] for a full account of the experimental details, including the hydrogen charging procedure.

Figures 2-4 show the dependence of experimental fracture stress, σ_f, on diffusible hydrogen content, H_D, for the notched round specimens with different notch root radii obtained by Wang et al. [15, 16, 17] for steels 4135A and 4135B, and the boron-alloyed steel. In these plots, the fracture stress is defined as $\sigma_f = F_{max}/A_{0-net}$, in which F_{max} represents the maximum tensile load attained in the tests and A_{0-net} is the initial cross-section net area of the notch. Further, it proves convenient to conduct a power law fitting of the experimental results, as indicated by the lines displayed in the figures, in the form $\sigma_f = kH_D^m$, where k and m are constants. Table 1 provides parameters k and m for each set of experimental data. Observe that the fracture stress decreases rather dramatically, particularly for the notched specimens with smaller radius, ρ, with only a small amount of hydrogen content. For example, in the case of steel 4135 A and $\rho = 0.1$ mm, the fracture stress decreases from $\sigma_f \approx 1800$ MPa at $H_D \approx 0.1$ wppm to $\sigma_f \approx 1000$ MPa at $H_D \approx 0.3$ wppm, as as indicated in Fig. 2. The variation of σ_f with H_D for steel 4135 B and $\rho = 0.1$ mm is even more severe, as can be seen in Fig. 2. Essentially similar trends are also observed for the results of the boron-alloyed steel shown in Fig. 4.

4 Computational Procedures

4.1 Finite Element Models

Numerical simulations were performed for detailed 3-D finite element models of the notched tensile specimens previously described to measure the effects of hydrogen embrittlement on

fracture strength. The 3-D finite element mesh for the notch round tensile specimen with a root radius of $\rho = 0.25$ mm is displayed in Fig. 5(a-b). The grip conditions are enforced by appropriate constraints in the X and Y directions on nodes located at $Z = L_g/2$. The geometry and loading configuration creates symmetry conditions that permit the use of only one-quarter, 3-D model of the tensile specimens in which displacement controlled loading, as shown in Fig. 5(a), permits extending the numerical computations beyond the maximum load attained in the simulations.

This 3-D finite element model consists of 45,707 nodes 41,716 8-node elements with a more refined mesh describing the notch root region, as displayed in Fig. 5(b). Here, the notch root geometry is modeled by an element size of ≈ 0.02 mm over distances along the net section radius of $\approx 20 \times \rho$ to resolve accurately the stress and strain distribution ahead of the notch. Essentially similar mesh arrangements are used for other 3-D finite element models of the notched tensile specimens having radius $\rho = 0.1$ and 0.8 mm - to conserve space, they are not included here.

4.2 Constitutive Model and Hydrogen-Related Parameters

The hydrogen-coupled material model adopted extends a conventional J_2 flow theory with Mises plastic potential to include the effects of solute hydrogen on the flow properties in large geometry change (LGC) setting. Since hydrogen does affect the macroscopic tensile behavior of unnotched specimens [16], the uniaxial (tensile) stress-strain response for the material can be represented by a power-hardening model in the form

$$\frac{\bar{\epsilon}}{\epsilon_{ys}} = \frac{\bar{\sigma}}{\sigma_{ys}} \quad , \quad \bar{\epsilon} \leq \epsilon_{ys} \qquad ; \qquad \frac{\bar{\epsilon}}{\epsilon_{ys}} = \left(\frac{\bar{\sigma}}{\sigma_{ys}}\right)^n \quad , \quad \bar{\epsilon} > \epsilon_{ys} \tag{11}$$

where $\bar{\sigma}$ defines the uniaxial true stress, $\bar{\epsilon}$ denotes the logarithmic strain, σ_{ys} and ϵ_{ys} are the reference (yield) stress and strain, and n denotes the strain hardening exponent. For the materials under discussion and using the mechanical data reported in Wang et al. [15, 16, 17], the following properties are adopted: 1) $\sigma_{ys} = 1235$ MPa, $\sigma_{uts} = 1320$ MPa and $n = 28$ for steel 4135A; 2) $\sigma_{ys} = 1320$ MPa, $\sigma_{uts} = 1450$ MPa and $n = 22$ for steel 4135B and 3) $\sigma_{ys} = 1160$ MPa, $\sigma_{uts} = 1305$ MPa and $n = 19$ for the boron-alloyed steel. Here, σ_{uts} represents the tensile strength for the materials and the strain hardening exponent, n, is conveniently estimated from API 579 [25]. Moreover, the analyses also consider the elastic modulus, $E = 206$ GPa and Poisson's ratio, $\nu = 0.3$.

Within the context of finite strain solutions, the Mises yield surface is described in terms of Cauchy (true) stresses, which in turn are in equilibrium with hydrogen. The local fields of hydrostatic stress and plastic strain then determine the total hydrogen concentration, as given

in previous Eq. (7). The finite element code WARP3D [21] provides the numerical solutions for the 3-D analyses of the notched tensile specimens reported here. Readers are referred to WARP3D user manual for a full account of the constitutive framework and numerical procedures incorporating Mises plasticity in the presence of hydrogen.

To generate the 3-D numerical solutions needed to evaluate the influence of hydrogen on the mechanical behavior for the notched tensile specimens, the hydrogen-model parameters described in Section 2 should be appropriately chosen to reflect the kinetics of hydrogen diffusion for the high strength steels employed in our study. Unfortunately, Wang et al. [15, 16, 17] do not provide detailed information on the hydrogen-related parameters for their materials, other than standards values such as the partial molar volume of hydrogen in bcc-Fe. However, reasonably good estimates for the required parameters are obtainable from the work of Novak et al. [26], who reported a study of hydrogen-induced intergranular fracture in a quenched and tempered AISI 4340 steel with 1490 MPa of yield stress. To the extent that those hydrogen-related parameters can be regarded as phenomenological quantities chosen to approximately describe the effects of hydrogen on the flow properties, small parameter variations are compensated by corresponding changes in the content of hydrogen which is in equilibrium with the local fields of hydrostatic stress and plastic strain, so that they are seen not of great influence in the fracture strength predictions addressed here. Thus, we proceed to define the following parameters based on the work of Novak et al. [26]: partial molar volume of hydrogen, $V_H = 2.1 \times 10^{-6}\,\mathrm{m}^3/\mathrm{mol}$, molar volume of the host metal (Fe), $V_M = 7.11 \times 10^{-6}\,\mathrm{m}^3/\mathrm{mol}$, number of sites per trap, $\alpha = 1$, number of NILS per solvent atom, $\beta = 1$, and the trap binding energy, $W = -18\,\mathrm{kJ/mol}$. This latter parameter is also within the values reported by Ayas et al. [27].

5 Results and Discussion

The following sections provide the essential results derived from the 3-D analyses incorporating effects of hydrogen on the fracture strength for the notched tensile specimens discussed previously. The presentation begins with descriptions of variations in key quantities ahead of the notch in connection with notch radius for uncharged and hydrogen-charged specimens, which have a direct bearing on the mechanical behavior of the specimens. Further, these features are central to establish of a local stress criterion describing effects of hydrogen embrittlement on fracture strength. Then we turn attention to predictions of the notch tensile strength dependence on hydrogen content based on the proposed fracture criterion.

5.1 Uncharged Notched Tensile Specimens

Before launching into the analysis of the fracture response for the hydrogen-charged notch round tensile specimens, we briefly address some general aspects of the mechanical behavior of uncharged specimens (with no hydrogen) which have a bearing on the predictions of fracture strength described later. Specifically, we are interested in examining the evolution of hydrostatic stress and plastic strain with increased loading ahead of the notch. Recall that the local hydrogen concentration and, thus, hydrogen-induced degradation, is coupled with the magnitude and distribution of these quantities, so that a strong interplay between fracture strength and notch radius may be expected from these results.

Figures 6-7 show the distributions of hydrostatic stress, σ_h, and effective plastic strain, ϵ_p, in the radial direction ahead of notch for the notched specimens with $\rho = 0.1$ and 0.8 mm at different load levels, in which σ_h is conventionally defined as the average of the three principal stresses, σ_k with $k = 1, 2, 3$, given by $(\sigma_1 + \sigma_2 + \sigma_3)/3$. In this plots, the load level is characterized by the applied net stress, $\sigma_{net} = F/A_{0-net}$, where F is the current load, and takes on three values: $\sigma_{net} = 1000$, 1500 and 2000 MPa - the latter load approximately corresponds to the failure load for the uncharged specimens of steel 4135A reported by Wang et al. [15]. The strong effect of notch radius on the evolution of hydrostatic stress and plastic strain with increased loading is evident. First, compare the stress results for $\rho = 0.1$ mm with those for $\rho = 0.8$mm displayed in Figs. 6(a) and 7(a). At every load level considered, the peak stress for $\rho = 0.1$ mm is significantly higher and associated with a very rapid increase over a relatively smaller distance in comparison with the corresponding value for $\rho = 0.8$ mm. Now, direct attention to the distribution of plastic strains shown in Figs. 6(b) and 7(b). As could be expected, much larger plastic strains are observed close to the notch for the specimen with $\rho = 0.1$ mm. These trends are consistent with previous studies (see, for example, [15, 28]) in that an increased notch radius, which is associated with reduced stress triaxiality, reduces the magnitude of stresses and strains ahead of notch. More importantly, though, because of the coupling between stress triaxiality and hydrogen concentration, these features have arguably important implications on the fracture behavior of hydrogen-charged specimens and provide the motivation to introduce a local stress-based criterion as addressed next.

5.2 Hydrogen Content and Principal Stress Distribution Ahead of Notch

Figures 8-11 provide descriptions of maximum principal stress, σ_1, and hydrogen concentration in NILS, c_L, for selected cases of the extensive finite element analyses for the notched tensile specimens that include the influence of hydrogen. These plots illustrate the coupled

effects of notch radius and total hydrogen content on the distributions of σ_1 and c_L for specimens with $\rho = 0.1$ mm and 0.8 mm at fracture for steel 4135A - refer to Fig. 2 shown previously. These notched tensile configurations exhibit widely different stress triaxialities in this study associated with the notch radius - $\rho = 0.1$ mm corresponds to the highest stress triaxiality (associated with a high stress concentration) while lower stress triaxiality conditions (connected with a lower stress concentration) exist for $\rho = 0.8$ mm. Use of these specimen geometries thus gives a fairly representative description of the key quantities controlling hydrogen-assisted fracture of the notched tensile specimens. Although not shown here in the interest of space, we note that the distributions of σ_1 and c_L that develop for the specimen with $\rho = 0.25$ mm are very similar to those shown in Figs. 8-11.

Consider first the distributions of σ_1 and c_L ahead of notch for the tensile specimen with $\rho = 0.1$ mm and two levels of total hydrogen content, $H_D = 0.25$ wppm and 2 wppm shown in Figs. 8(a-d). Here, observe that d represents the radial distance measured from the notch tip as illustrated in Fig. 1. The trends shown by these results are clear. An increase in hydrogen content is associated with substantial reduction in the peak stress ahead of the notch - note that the scale in Fig. 9(a) is different to accommodate the reduced stress level at much smaller notch tip distance. At lower hydrogen content, $H_D = 0.25$ wppm, Fig. 8(a) shows that the peak stress occurs over a narrow and pronounced region near the notch tip in connection with very steep stress gradients. This behavior is accompanied by a relatively smooth variation of the hydrogen concentration in NILS, in which c_L increases only slightly from the levels determined at distances far from the notch as seen in Fig. 8(b). By contrast, Figs. 9(a-b) exhibit different features as now the reduced peak stress is accompanied by the development of high levels of c_L over a much larger distance. Further observe that the location at which the peak values for both σ_1 and c_L occur essentially coincide - for $H_D = 0.25$ wppm, the maximum values of σ_1 and c_L occur at a notch tip distance, $d \approx 0.15$ mm.

Consider next the numerical results for the specimens with 0.8 mm and $H_D = 0.25$ wppm and 2 wppm displayed in Figs. 10 and 11. While the distributions of σ_1 and c_L ahead of notch are qualitatively similar, there are less pronounced and exhibit a less severe gradient, particularly in the case of the lower hydrogen content, $H_D = 0.25$ wppm. This latter feature is consistent with the expected stress development for a notched tensile specimen with a larger notch radius and, thus, lower stress concentration, which gives rise to a relatively more uniform stress distribution over the net section of the specimen - see the results presented in previous section. Moreover, also observe that, similarly to the previous case, the location at which the peak levels for σ_1 and c_L occur is coincident. These trends are consistent with the recent findings of Depover et al [29] in that there is a strong connection between the critical values of peak stress and hydrogen concentration that control unstable fracture in hydrogen

charged tensile specimens.

5.3 Local Stress Criterion to Predict Effects of Hydrogen Embrittlement

The analyses of the effects of notch radius and total hydrogen content on the distributions of σ_1 and c_L provide a basis to introduce a stress-based approach to assess the effects of hydrogen embrittlement on the fracture strength of notched tensile specimens. A simple criterion can now be derived by considering that fracture in the notched specimen occurs under a critical stress value associaed with a decreasing function of hydrogen content. Moreover, the combination of critical stress and hydrogen content should result in a failure criterion which is reasonably invariant to stress triaxiality, as characterized by the notch radius in the present context.

Figure 12 shows the dependence of peak value of maximum principal stress, σ_1, on maximum hydrogen concentration in NILS for the notched round specimens with different notch root radii derived from the previous numerical analyses including the influence of hydrogen for steel 4135A. Apart from small differences in principal stress values in the case of lower hydrogen concentration in NILS, a single power law relationship between σ_1 and c_L, which is fairly independent of notch radius, is evident in the plot. Much of the behavior associated with low contents of hydrogen can be explained in terms of the stresses that develop ahead of a notch for this type of tensile geometry. When the hydrogen content is low, say $H_D = 0.25$ wppm, for which material degradation is still not so severe, the notch stresses need to build up to a higher value before unstable fracture becomes possible. Under this condition, the notch radius plays a more prominent role as the stresses near the notch tip approximately inversely scales with ρ and are, thus, more sensitive to the mesh resolution, particularly in the case of $\rho = 0.1$ mm. Since our primary interest lies in exploring an engineering-level application of a stress-based criterion to predict effects of hydrogen embrittlement, the option of determining an optimum mesh for each specimen geometry was not pursued here, as the mesh resolution used in the present analyses proved highly satisfactory for all notched geometries. Moreover, to the extent that those small variation at low contents of hydrogen are of no major influence, the results displayed in Fig. 12 provide a convincing case to establish a valid failure locus for the material under consideration.

5.4 Fracture Strength Predictions

To verify the applicability of the local stress criterion introduced above in terms of a failure locus defining fracture conditions, this section describes predictions of the fracture strength

dependence on hydrogen content for the experimental tests performed on two different high strength steels by Wang et al. [16, 17] shown previously (refer to Section 3). Here, we seek to determine a functional form of σ_1 with c_L for the specimen with a notch radius of $\rho = 0.8$ mm, which is assumed to describe the failure locus for the material. By postulating independence of such a locus on specimen geometry, as characterized by the notch radius, the variation of the fracture strength, σ_f, with diffusible hydrogen content, H_D, for other notched specimens with different notch root radii can then be rationally predicted. Because notched specimens with varying notch root radii correlate directly with different levels of stress triaxiality, quantitative estimates of the σ_f vs. H_D relation for specimens with $\rho = 0.1$ mm are representative of predictions of the effects of hydrogen embrittlement in a large class of structural components, including, for example, the high strength fasteners for marine and subsea applications discussed in the introduction.

Figure 13 gives the prediction of fracture strength, σ_f, with increased content of diffusible hydrogen content, H_D, for steel 4135B. First, consider determination of the failure locus for this material displayed in Fig. 13(a). Using the dependence of peak value of maximum principal stress on maximum hydrogen concentration in NILS at fracture for the notched round specimen with $\rho = 0.8$ mm, a relationship in the form of $\sigma_1 = 435.5 c_L^{-0.148}$, with σ_1 in MPa and c_L in H/mol, describes well the critical combination of σ_1 and c_L that controls fracture of the notched specimen under different H_D-values. Now, direct attention to the fracture strength predictions for the notched specimen with $\rho = 0.1$ mm displayed in Fig. 13(b). In this plot, the solid symbols represent the experimental data obtained by Wang et al. [16] (refer also to Section 3) whereas the solid line defines the variation σ_f with H_D predicted from the failure locus determined for the specimen with $\rho = 0.8$ mm. The effect of hydrogen embrittlement on the fracture strength for this material is seen to be accurately predicted by the failure locus based on the local stress criterion.

Predictions of hydrogen effects on fracture for the boron-alloyed steel further illustrate the effectiveness of the proposed local stress criterion. Figure 14 shows the predicted dependence of σ_f on H_D for this material using the same procedure just outlined, in which the failure locus for this material displayed in Fig. 14(a) is obtained from the notched specimens with $\rho = 0.8$ mm. Similarly to the previous case, apart from some small deviations most likely associated with the inherent scatter in experimental data, the quality of the fracture strength predictions is evident in the plot shown in Fig. 14(b).

6 Summary and Conclusions

The 3-D finite element analyses of hydrogen-charged tensile specimens incorporating a hydrogen transport model to quantify the effects of dissolved hydrogen concentration on the mechanical behavior of quenched and tempered, high strength steels provided quantitative estimates of macroscopic embrittlement of notched round specimens with different notch root radii. The numerical simulations conducted here demonstrated that the coupling between stress triaxiality and hydrogen concentration has important implications on the fracture behavior of hydrogen-charged specimens, which, in turn, provides strong support to the adoption of a failure criterion in terms of achieving a critical level of tensile stress over the vicinity of the notch tip coupled to changes in local hydrogen concentration. The local stress criterion is translated into a failure locus, which is assumed independent of notch radius and, thus, stress triaxiality.

The verification studies conducted here utilized experimentally measured values of fracture strength generated from tests of notched round tensile specimens in the presence of hydrogen for three quenched and tempered, high strength steels with yield stress in the range of $1160 \sim 1320$ MPa. The experimental tests included notched specimens with radius of $\rho = 0.1$, 0.25 and 0.8 mm. For the cases analyzed here, construction of a failure locus based on a critical combination of maximum principal stress and hydrogen concentration enabled predictions of fracture strength for hydrogen-charged tensile specimens which are in very good agreement with experimental data. Overall, the results presented here lend additional support for further developments of a local criterion incorporating a relatively simple hydrogen transport model to predict hydrogen embrittlement effects on the fracture strength of high strength steels.

Acknowledgments

This investigation was supported by grants principally from the São Paulo Research Foundation (FAPESP) through Grant $2022/00307-8$, and through a Research Fellowship from the Brazilian Council for Scientific and Technological Development (CNPq) through Grant $302853/2018-9$ for the first author (CR). The authors acknowledge Petrobras for providing additional support for the work described here.The authors are also indebted to Luís G. T. S. Leite and Daniel C. F. Ferreira (Petrobras Research Center - CENPES) for the helpful discussions and encouragement to conduct this work.

References

[1] O. Barrera, D. Bombac, Y. Chen, T. D. Daff, E. Galindo-Nava, P. Gong, D. Haley, R. Horton, I. Katzarov, J. R. Kermode, C. Liverani, M. Stopher, F. Sweeney, Understanding and mitigating hydrogen embrittlement of steels: A review of experimental, modelling and design progress from atomistic to continuum, Journal of Materials Science 53 (2018) 6251–6290.

[2] R. P. Gangloff, Hydrogen assisted cracking of high strength alloys, in: R. R. I. Milne, B. Karihaloo (Eds.), Comprehensive Structural Integrity, Vol. 6, Elsevier Science, 2003, pp. 31–101.

[3] J. A. Ronevich, E. J. Song, B. P. Somerday, C. W. S. Marchi, Hydrogen-assisted fracture resistance of pipeline welds in gaseous hydrogen, International Journal of Hydrogen Energy 46 (2021) 7601–7614.

[4] American Society for Testing and Materials, Standard specification for precipitation-hardening and cold worked nickel alloy bars, forgings, and forging stock for moderate or high temperature service, ASTM B637-15 (2015).

[5] K. A. Esaklul, T. M. Ahmed, Prevention of failures of high strength fasteners in use in offshore and subsea applications, Engineering Failure Analysis 16 (2009) 1195–1202.

[6] American Petroleum Institute, Alloy and carbon steel bolting for use in the petroleum and natural gas industries, API Specification 20E (2019).

[7] American Petroleum Institute, Corrosion resistant bolting for use in the petroleum and natural gas industries, API Specification 20F (2021).

[8] International Organization for Standardization, Petroleum and natural gas industries - materials for use in H_2S-containing environments in oil and gas production: Part 2: Cracking-resistant carbon and low-alloy steels, and the use of cast irons, ISO 15156-2-2020 (2020).

[9] M. Iannuzzi, A. Barnoush, R. Johnsen, Materials and corrosion trends in offshore and subsea oil and gas production, Materials Degradation 1 (2), https://doi.org/10.1038/s41529-017-0003-4.

[10] M. Dadfarnia, A. Nagao, S. Wang, M. L. Martin, B. P. Somerday, P. Sofronis, Recent advances on hydrogen embrittlement of structural materials, International Journal of Fracture 196 (2015) 223–243.

[11] A. R. Troiano, The role of hydrogen and other interstitials in the mechanical behavior of metals (1959 Edward De Mille Campbell Memorial Lecture), Transactions of American Society for Metals 52 (1960) 54–80.

[12] R. A. Oriani, A mechanistic theory of hydrogen embrittlement of steels, Berichte der Bunsengesellschaft für physikalische Chemie 76 (1972) 848–857.

[13] C. Beachem, A new model for hydrogen-assisted cracking (hydrogen embrittlement), Metallurgical Transactions 3 (2) (1972) 441–455.

[14] H. K. Birnbaum, P. Sofronis, Hydrogen-enhanced localized plasticity - a mechanism for hydrogen-related fracture, Materials Science and Engineering A176 (1994) 191–202.

[15] M. Wang, E. Akiyama, K. Tsuzaki, Effect of hydrogen and stress concentration on the notch tensile strength of aisi 4135 steel, Materials Science and Engineering A 398 (2005) 37–46.

[16] M. Wang, E. Akiyama, K. Tsuzaki, Effect of hydrogen on the fracture behavior of high strength steel during slow strain rate test, Corrosion Science 49 (2007) 4081–4097.

[17] M. Wang, E. Akiyama, K. Tsuzaki, Fracture criterion for hydrogen embrittlement of high strength steel, Materials Science and Technology 22 (2) (2006) 167–172.

[18] R. A. Oriani, The diffusion and trapping of hydrogene in steel, Acta Metallurgica 18 (1) (1970) 147–157.

[19] P. Sofronis, R. M. McMeeking, Numerical analysis of hydrogen transport near a blunting crack tip, Journal of Mechanics and Physics of Solids 37 (1989) 317–350.

[20] P. Sofronis, Y. Liang, N. Aravas, Hydrogen induced shear localization of the plastic flow in metals and alloys, European Journal of Mechanics A 20 (2001) 857–872.

[21] B. Healy, A. Gullerud, K. Koppenhoefer, A. Roy, S. RoyChowdhury, J. Petti, M. Walters, B. Bichon, K. Cochran, A. Carlyle, J. Sobotka, M. Messner, R. H. Dodds, WARP3D: 3-D nonlinear finite element analysis of solids for fracture and fatigue processes, Tech. rep., University of Illinois at Urbana-Champaign, http://code.google.com/p/warp3d (2014).

[22] A. Taha, P. Sofronis, A micromechanis approach to the study of hydrogen transport and embrittlement, Engineering Fracture Mechanics 68 (2001) 803–837.

[23] R. A. Oriani, P. H. Josephic, Equilibrium aspects of hydrogen-induced cracking of steels, Acta Metallurgica 22 (1974) 1065–1074.

[24] R. A. Oriani, P. H. Josephic, Equilibrium and kinetic studies of the hydrogen-assisted cracking of steel, Acta Metallurgica 25 (1977) 979–988.

[25] American Petroleum Institute, Fitness-for-service, API RP-579-1 & ASME FFS-1 (2016).

[26] P. Novak, R. Yuan, B. P. Somerday, P. Sofronis, R. O. Ritchie, A statistical, physical-based, micro-mechanical model of hydrogen-induced intergranular fracture in steel., Journal of the Mechanics and Physics of Solids 58 (2010) 206–226.

[27] C. Ayas, V. S. Deshpande, N. A. Fleck, A fracture criterion for the notch strength of high strength steels in the presence of hydrogen, Journal of the Mechanics and Physics of Solids 63 (2014) 80–93.

[28] J. G. Kumar, M. Nandagopal, P. Parameswaran, K. Laha, M. D. Mathew, Effect of notch root radius on tensile behaviour of 316L(N) stainless steel, Materials at Hight Temperature 31 (3) (2014) 239–248.

[29] T. Depover, S. Hertelé, K. Verbeken, The effect of hydrostatic stress on the hydrogen induced mechanical degradation of dual phase steel: A combined experimental and numerical approach, Engineering Fracture Mechanics 221 (106704).

Table Captions

1. Parameters k and m describing the power law fitting of experimental fracture stress versus hydrogen concentration for the tested high strength steels.

Figure Captions

1. Geometry of the notched tensile specimen employed in the fracture tests of the hydrogen charged AISI 4135 steels and boron-alloyed steel conducted by Wang et al. [15, 16, 17].

2. Dependence of notch tensile strength, σ_f, on diffusible hydrogen content, H_D, for notched round specimens with different notch root radii for steel 4135A measured by Wang et al. [15].

3. Effect of diffusible hydrogen content, H_D, on notch tensile strength, σ_f, for notched round specimens with different notch root radii for steel 4135B measured by Wang et al. [16]

4. Variation of notch tensile strength, σ_f, with diffusible hydrogen content, H_D, for the notched round specimens with different notch root radii for a high strength boron-alloyed steel measured by Wang et al. [17].

5. (a) 3-D finite element mesh for the notch round tensile specimens with a root radius of $\rho = 0.25\,\text{mm}$. (b) Meshing detail of the notch root region.

6. Computed distributions along the net section for the uncharged specimen with $\rho = 0.1\,\text{mm}$ at three levels of net stress, $\sigma_{net} = 1000$, 1500 and 2000 MPa: (a) hydrostatic stress, σ_h. (b) plastic strain. ϵ_p.

7. Computed distributions along the net section for the uncharged specimen with $\rho = 0.8\,\text{mm}$ at three levels of net stress, $\sigma_{net} = 1000$, 1500 and 2000 MPa: (a) hydrostatic stress, σ_h. (b) plastic strain. ϵ_p.

8. Numerical results in the radial direction ahead of the notch tip for the hydrogen charged specimen with $\rho = 0.1\,\text{mm}$ and $H_D = 0.25\,\text{wppm}$ at $\sigma_f = 1096\,\text{MPa}$: (a) Maximum principal stress, σ_1. (b) Hydrogen concentration in NILS, C_L.

9. Numerical results in the radial direction ahead of the notch tip for the hydrogen charged specimen with $\rho = 0.1\text{mm}$ and $H_D = 2\text{wppm}$ at $\sigma_f = 388\text{MPa}$: (a) Maximum principal stress, σ_1. (b) Hydrogen concentration in NILS, C_L.

10. Numerical results in the radial direction ahead of the notch tip for the hydrogen charged specimen with $\rho = 0.8$ mm and $H_D = 0.25$ wppm at $\sigma_f = 1923$ MPa: (a) Maximum principal stress, σ_1. (b) Hydrogen concentration in NILS, C_L.

11. Numerical results in the radial direction ahead of the notch tip for the hydrogen charged specimen with $\rho = 0.8$mm and $H_D = 2$wppm at $\sigma_f = 1031$MPa: (a) Maximum principal stress, σ_1. (b) Hydrogen concentration in NILS, C_L.

12. Dependence of peak value of maximum principal stress, σ_{pr}, on maximum hydrogen concentration in NILS for the notched round specimens with different notch root radii derived from the numerical analyses including the influence of hydrogen for steel 4135A.

13. Prediction of fracture strength, σ_f, with increased content of diffusible hydrogen content, H_D, for steel 4135B. (a) Failure locus derived from the analyses conducted on the notched specimen with $\rho = 0.8$ mm. (b) Predicted variation of σ_f with H_D for the notched specimen with $\rho = 0.1$ mm.

14. Prediction of fracture strength, σ_f, with increased content of diffusible hydrogen content, H_D, for the boron-alloyed steel. (a) Failure locus derived from the analyses performed on the notched specimen with $\rho = 0.8$ mm. (b) Predicted dependence of σ_f on H_D for the notched specimen with $\rho = 0.1$ mm.

Table 1

Material	ρ (mm)	K	m
Steel 4135A	0.1	548	-0.5
	0.25	783	-0.41
	0.8	1269	-0.3
Steel 4135B	0.1	470	-0.24
	0.8	930	-0.3
Boron Steel	0.1	566	-0.54
	0.25	868	-0.4
	0.8	1537	-0.16

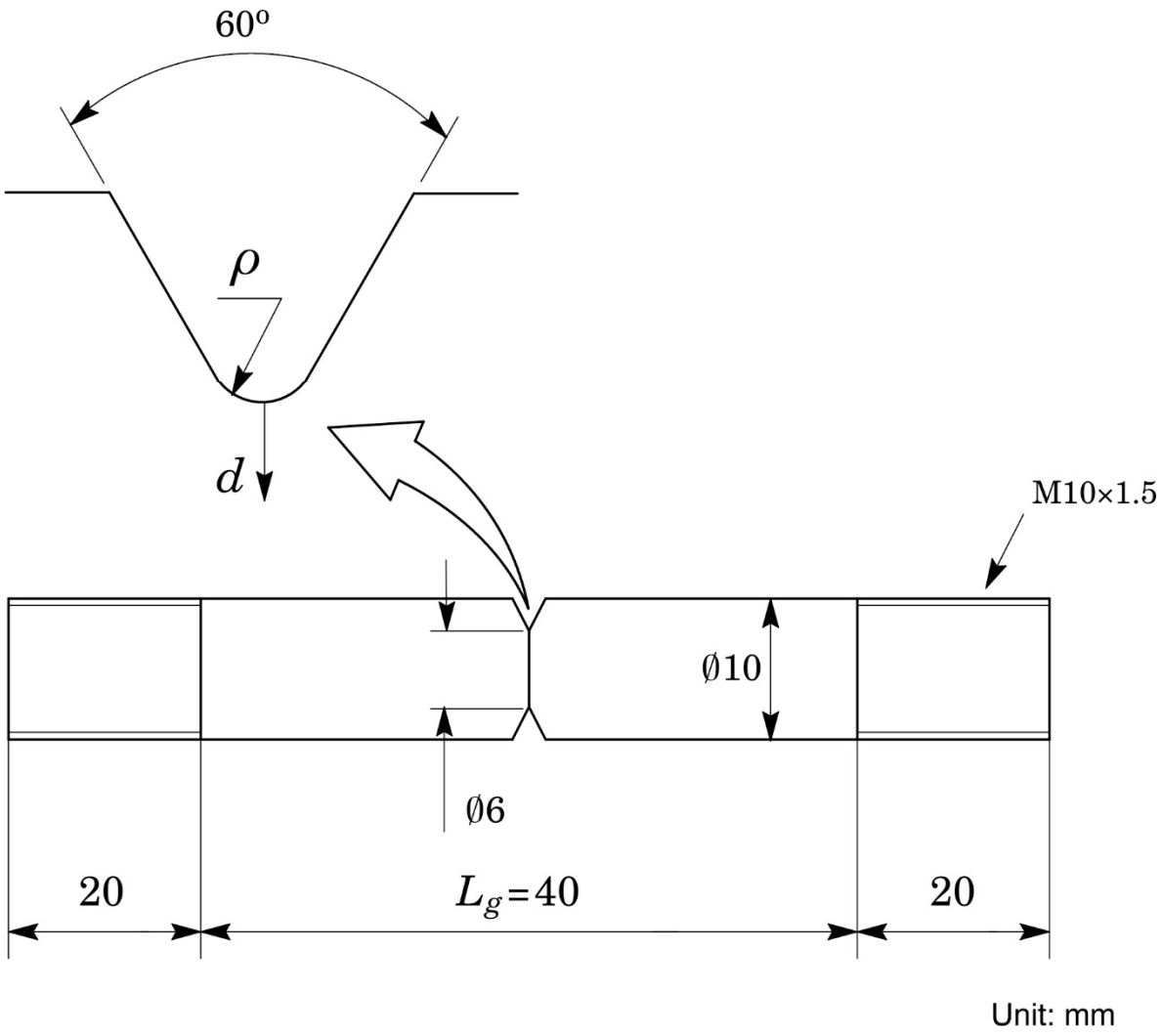

Figure 1

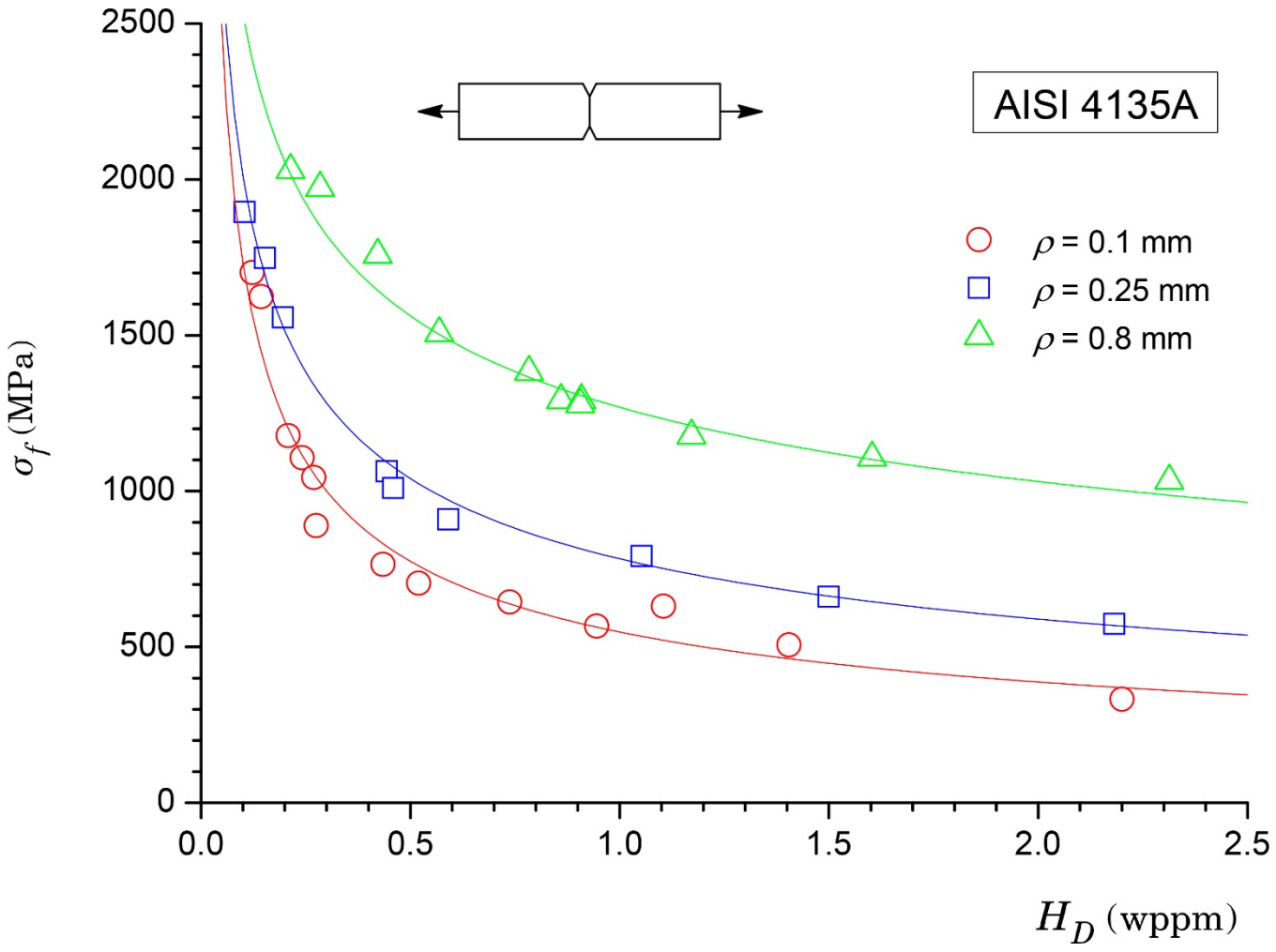
AISI 4135A
ρ = 0.1 mm
ρ = 0.25 mm
ρ = 0.8 mm
σf (MPa)
HD (wppm)
2500
2000
1500
1000
500
0
0.0
0.5
1.0
1.5
2.0
2.5

Figure 2

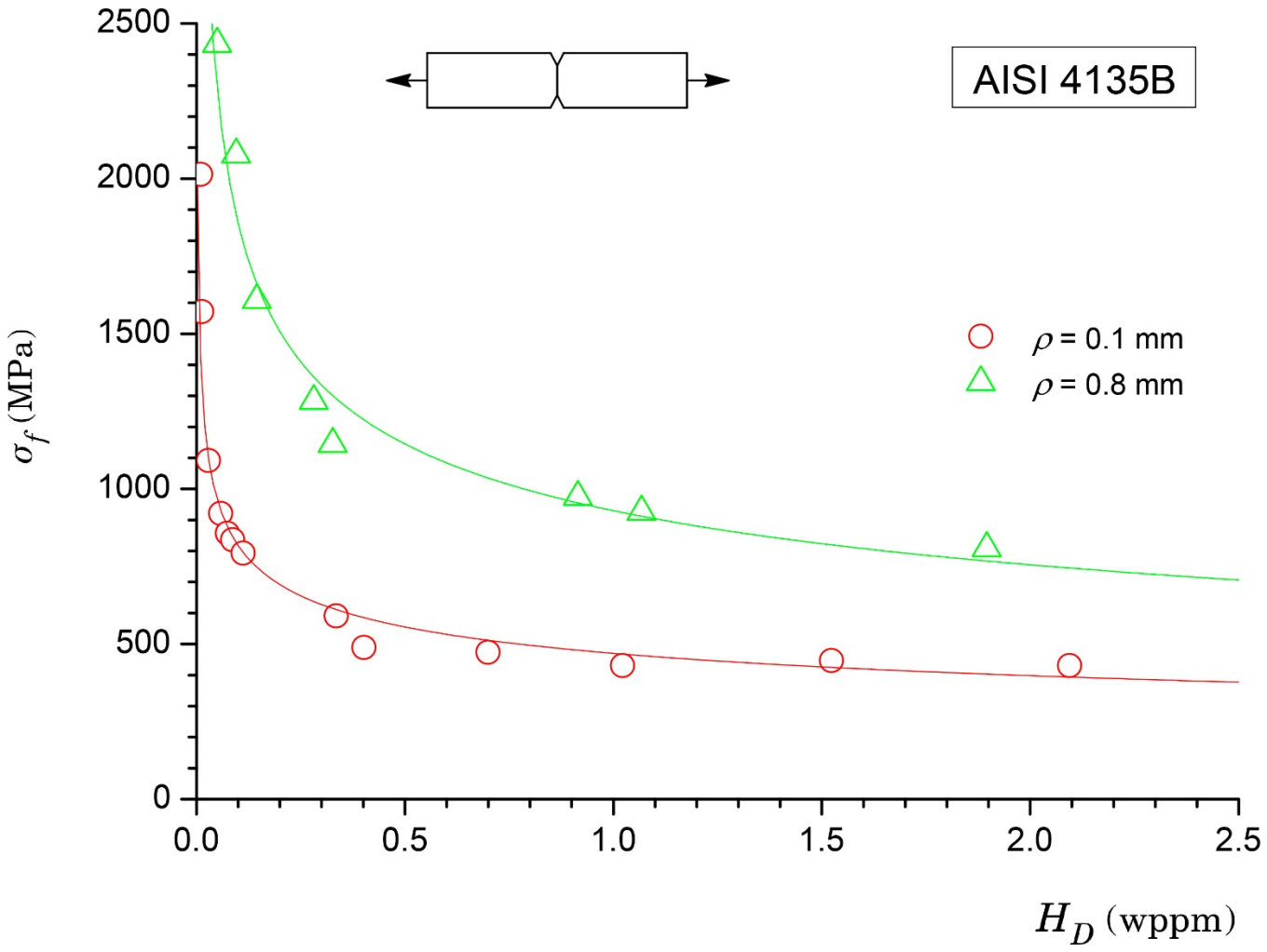
AISI 4135B
ρ = 0.1 mm
ρ = 0.8 mm
σf (MPa)
HD (wppm)
2500
2000
1500
1000
500
0
0.0
0.5
1.0
1.5
2.0
2.5

Figure 3

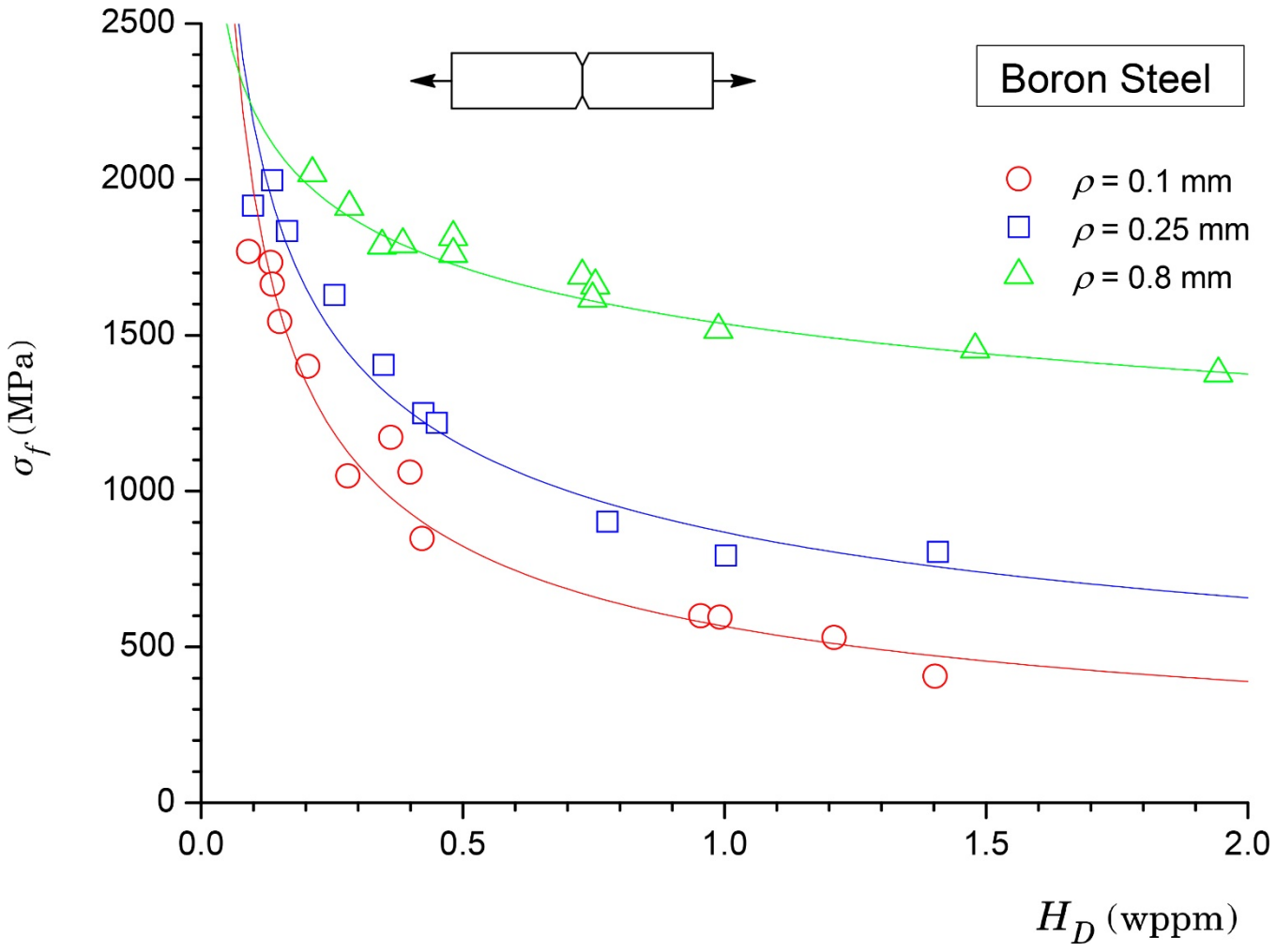
Boron Steel
ρ = 0.1 mm
ρ = 0.25 mm
ρ = 0.8 mm
σ_f (MPa)
H_D (wppm)
2500
2000
1500
1000
500
0
0.0
0.5
1.0
1.5
2.0

Figure 4

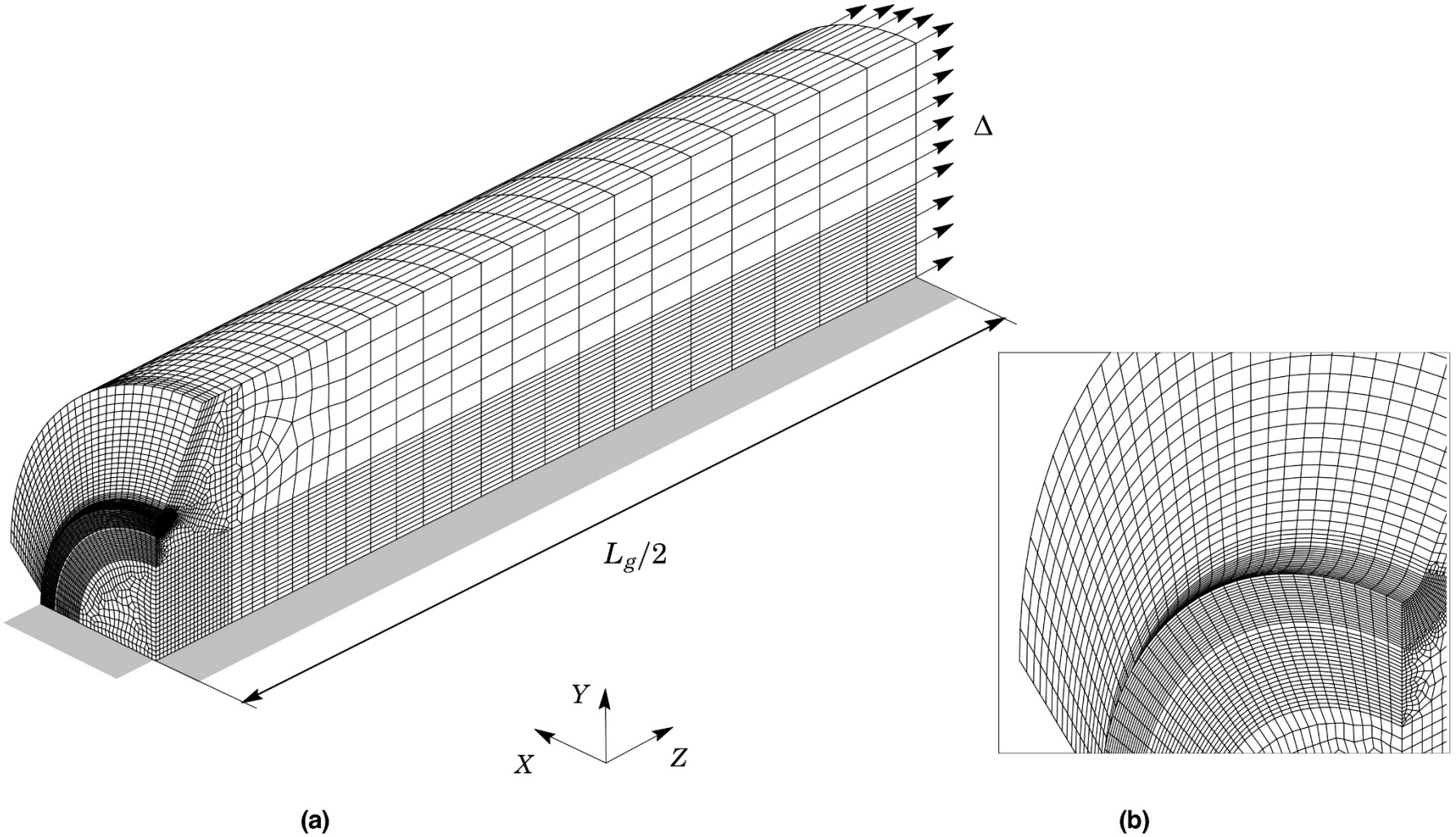

Figure 5

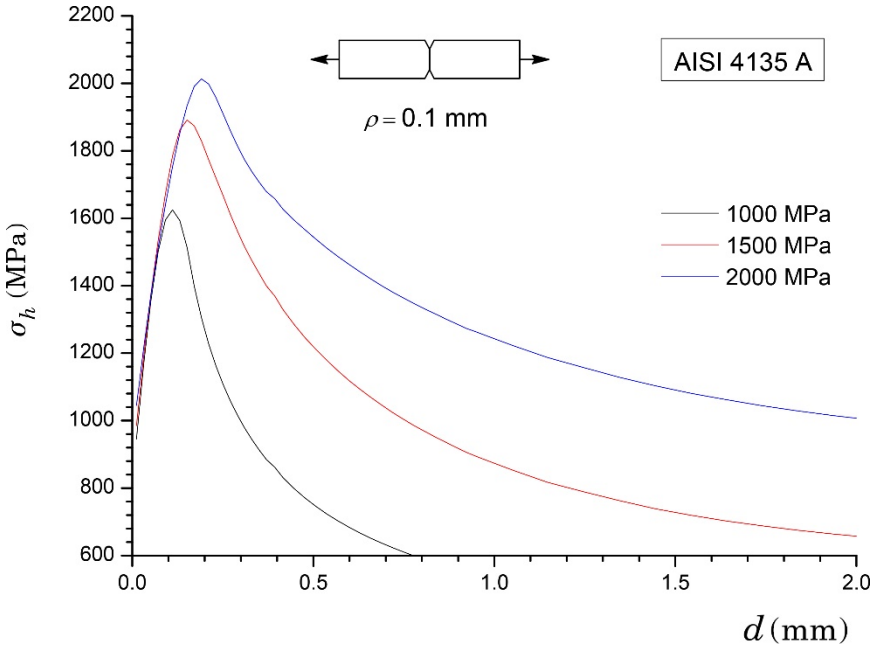
AISI 4135 A
$\rho = 0.1$ mm
1000 MPa
1500 MPa
2000 MPa
σ_h (MPa)
d (mm)
2200
2000
1800
1600
1400
1200
1000
800
600
0.0
0.5
1.0
1.5
2.0

(a)

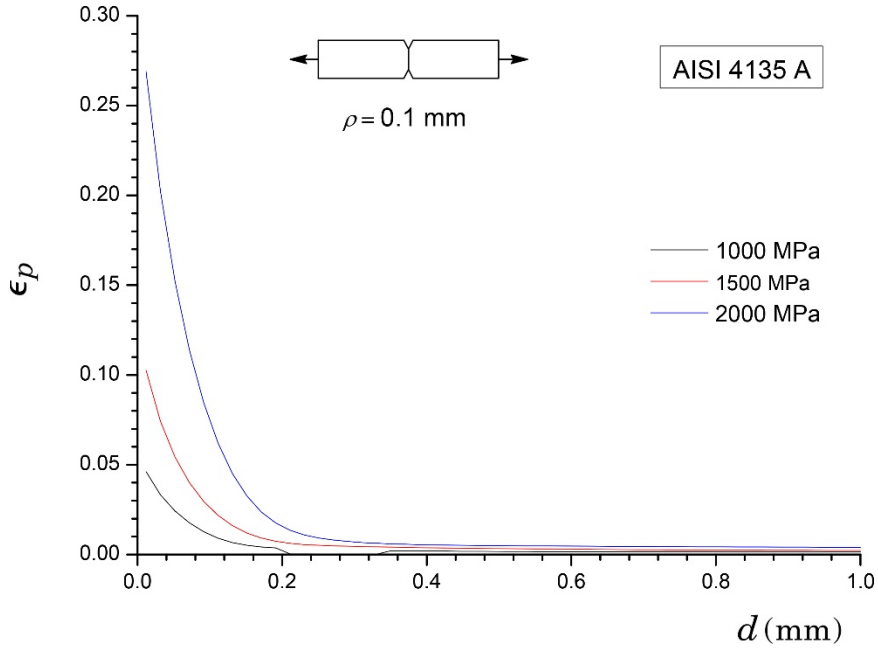
AISI 4135 A
$\rho = 0.1$ mm
1000 MPa
1500 MPa
2000 MPa
ϵ_p
d (mm)
0.30
0.25
0.20
0.15
0.10
0.05
0.00
0.0
0.2
0.4
0.6
0.8
1.0

(b)

Figure 6

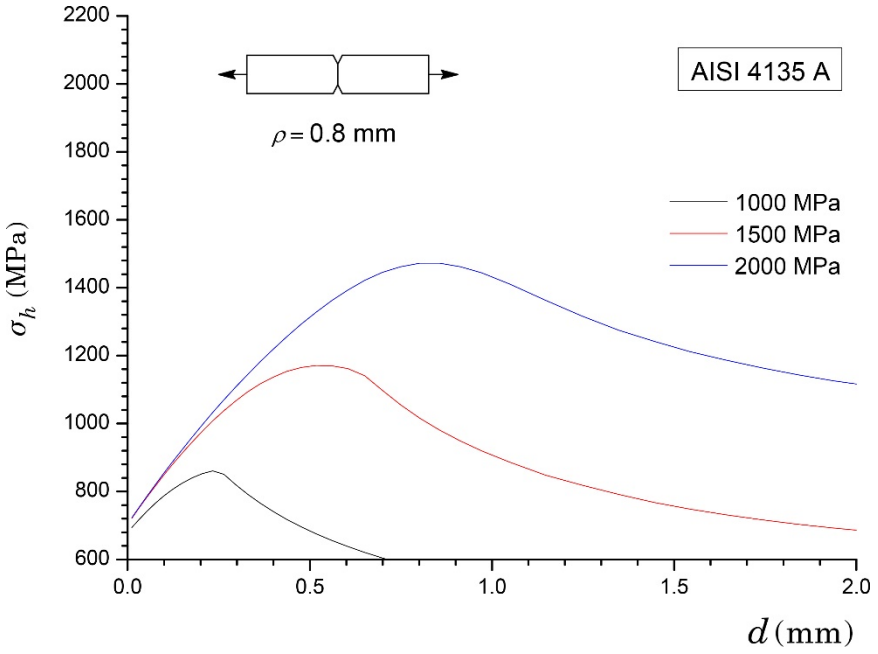
AISI 4135 A
ρ = 0.8 mm
1000 MPa
1500 MPa
2000 MPa
σh (MPa)
d (mm)
2200
2000
1800
1600
1400
1200
1000
800
600
0.0
0.5
1.0
1.5
2.0

(a)

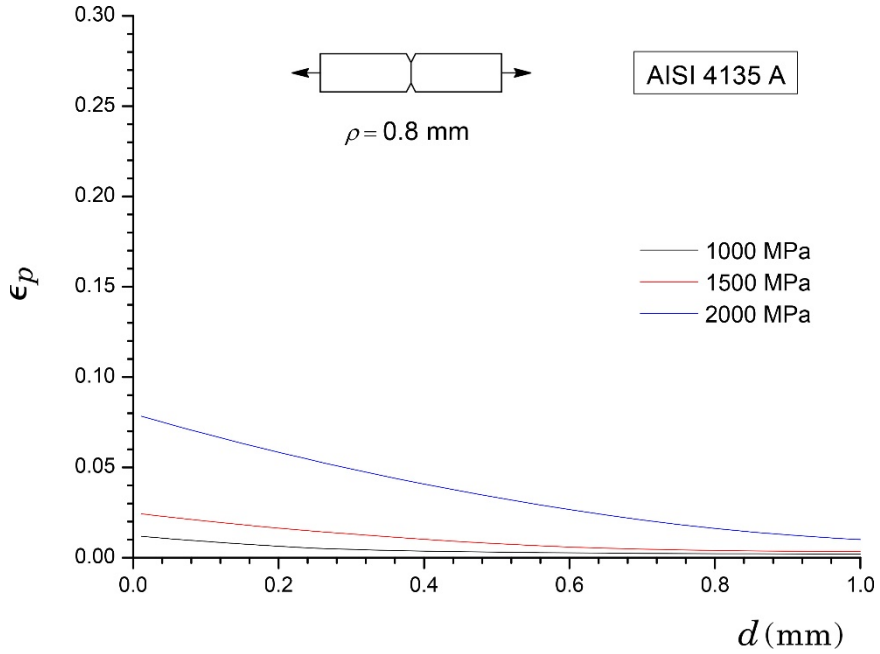
AISI 4135 A
ρ = 0.8 mm
1000 MPa
1500 MPa
2000 MPa
εp
d (mm)
0.30
0.25
0.20
0.15
0.10
0.05
0.00
0.0
0.2
0.4
0.6
0.8
1.0

(b)

Figure 7

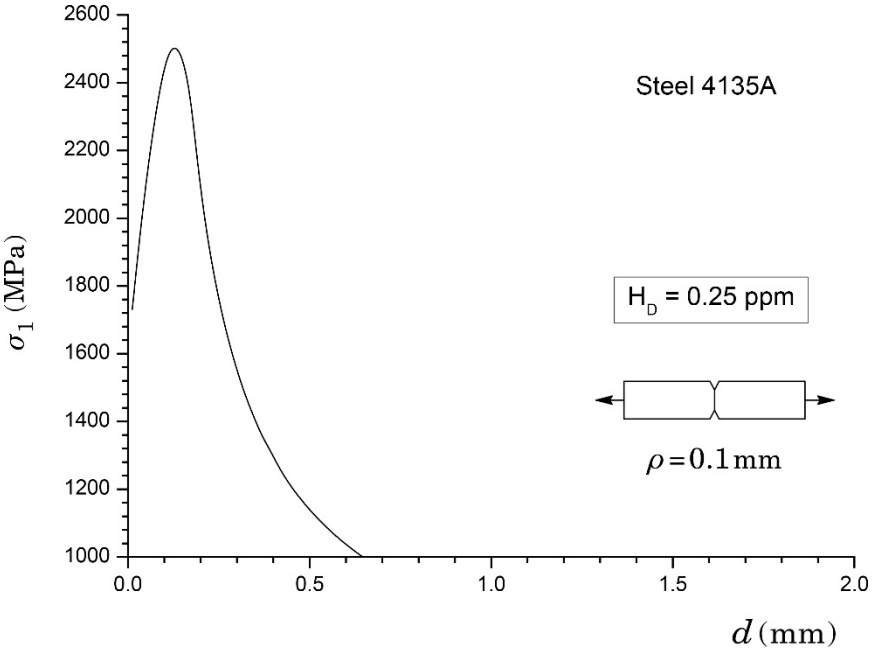
Steel 4135A
H_D = 0.25 ppm
$\rho = 0.1\,\mathrm{mm}$
σ_1 (MPa)
d (mm)
2600
2400
2200
2000
1800
1600
1400
1200
1000
0.0
0.5
1.0
1.5
2.0

(a)

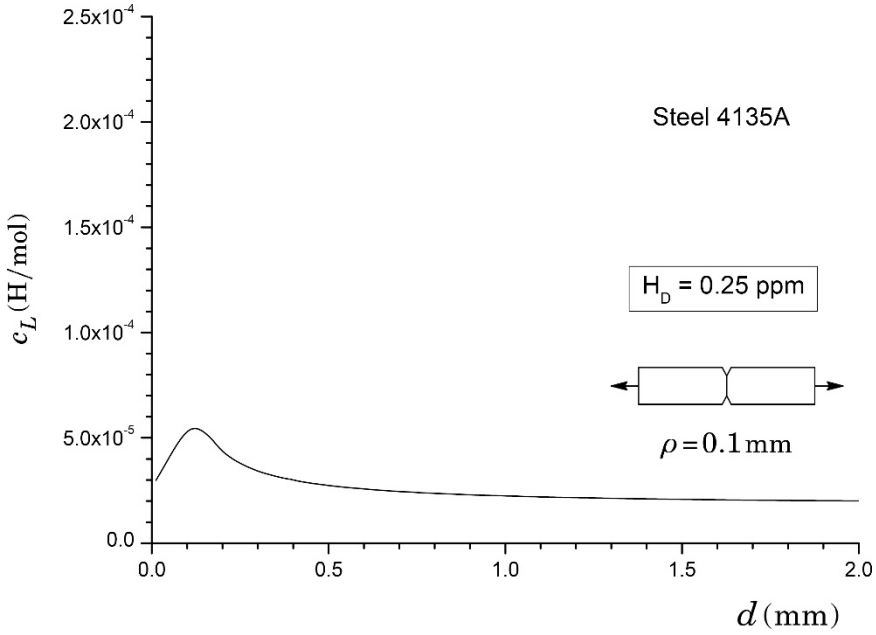
Steel 4135A
H_D = 0.25 ppm
$\rho = 0.1\,\mathrm{mm}$
c_L (H/mol)
d (mm)
2.5×10^{-4}
2.0×10^{-4}
1.5×10^{-4}
1.0×10^{-4}
5.0×10^{-5}
0.0
0.5
1.0
1.5
2.0

(b)

Figure 8

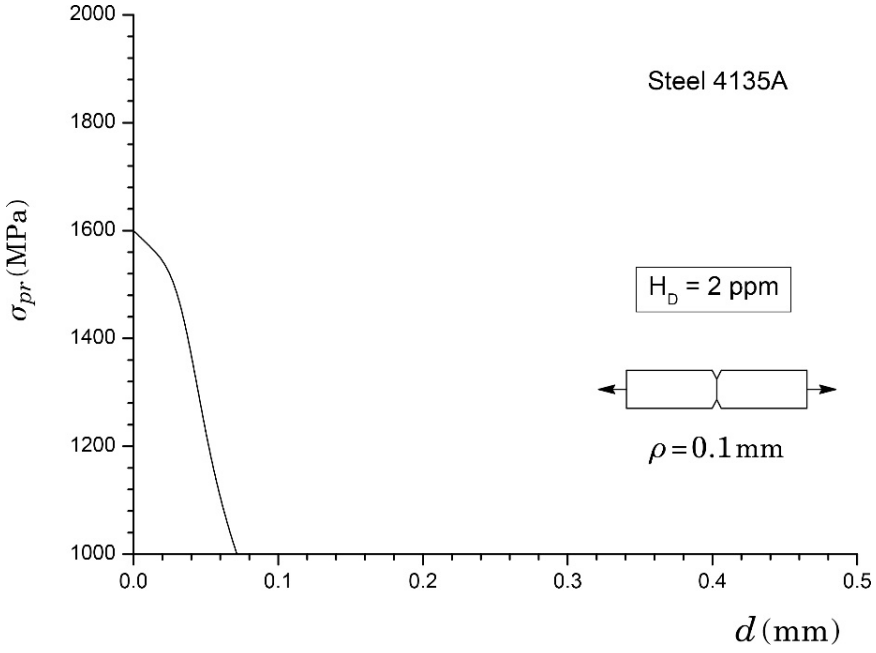
Steel 4135A
H_D = 2 ppm
$\rho = 0.1\,\mathrm{mm}$
σ_{pr} (MPa)
d (mm)
2000
1800
1600
1400
1200
1000
0.0
0.1
0.2
0.3
0.4
0.5

(a)

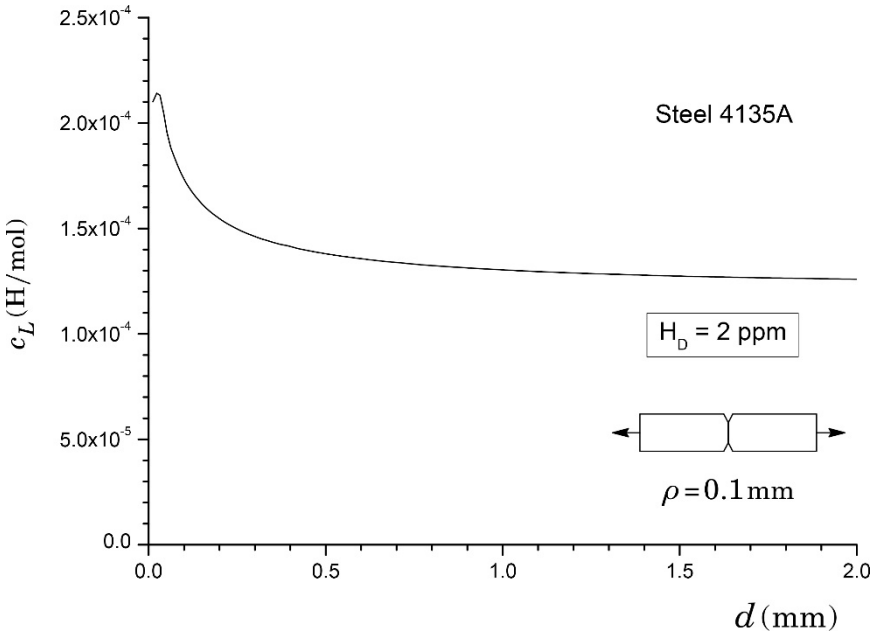
Steel 4135A
H_D = 2 ppm
$\rho = 0.1\,\mathrm{mm}$
c_L (H/mol)
d (mm)
2.5×10^{-4}
2.0×10^{-4}
1.5×10^{-4}
1.0×10^{-4}
5.0×10^{-5}
0.0
0.0
0.5
1.0
1.5
2.0

(b)

Figure 9

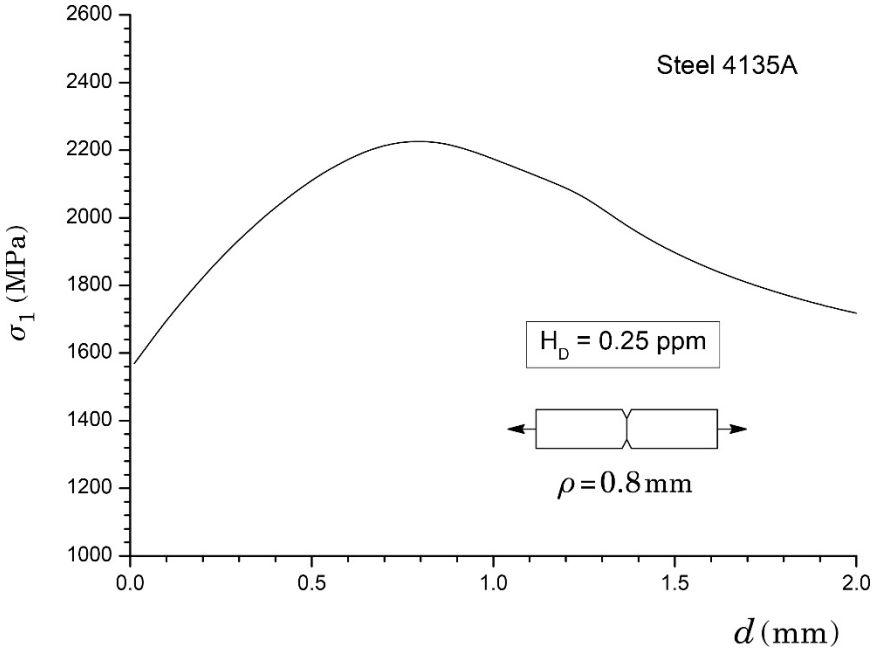
Steel 4135A
σ_1 (MPa)
2600
2400
2200
2000
1800
1600
1400
1200
1000
0.0
0.5
1.0
1.5
2.0
d (mm)
H_D = 0.25 ppm
$\rho = 0.8$ mm

(a)

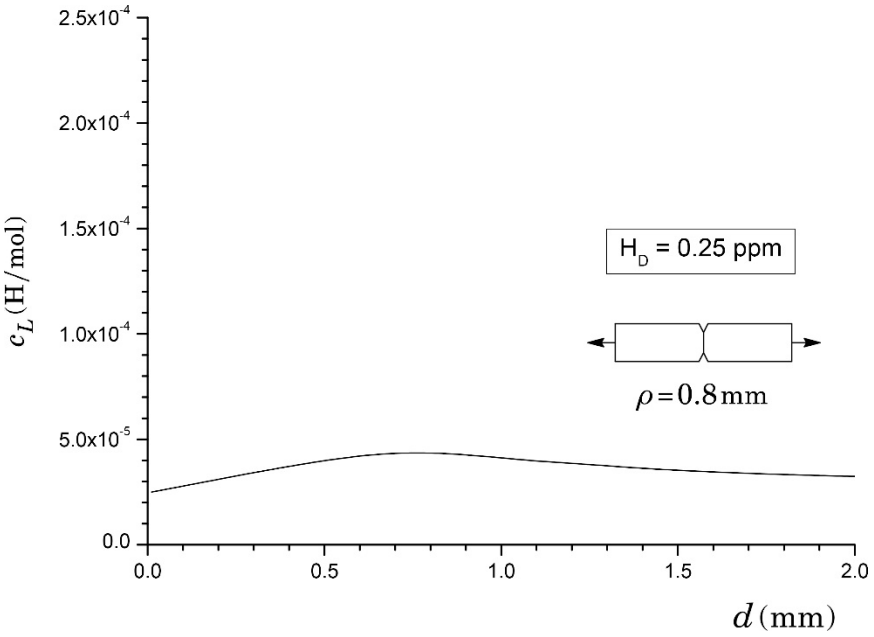
c_L (H/mol)
2.5x10^{-4}
2.0x10^{-4}
1.5x10^{-4}
1.0x10^{-4}
5.0x10^{-5}
0.0
0.0
0.5
1.0
1.5
2.0
d (mm)
H_D = 0.25 ppm
$\rho = 0.8$ mm

(b)

Figure 10

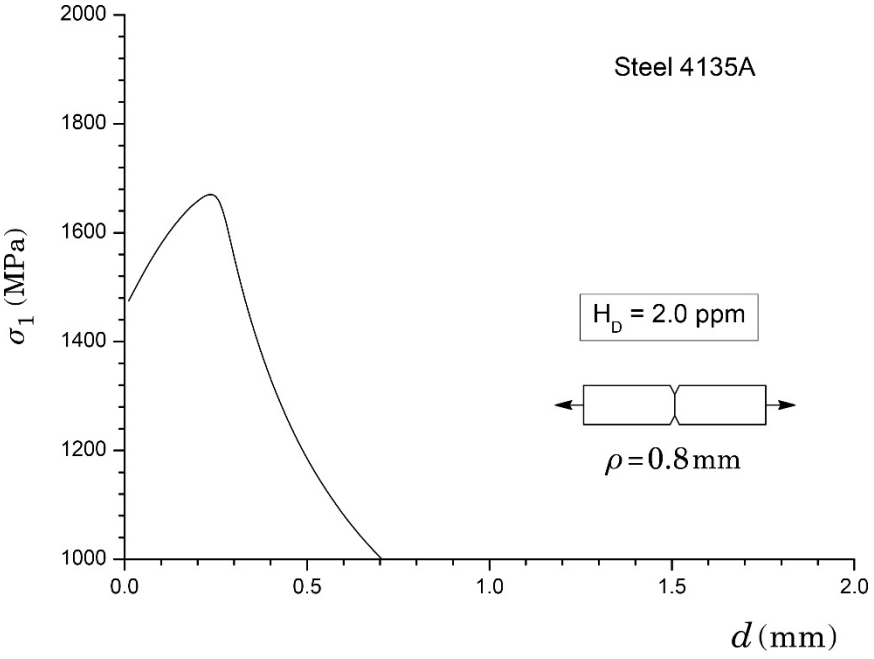
Steel 4135A
H_D = 2.0 ppm
$\rho = 0.8\,\mathrm{mm}$
σ_1 (MPa)
d (mm)
2000
1800
1600
1400
1200
1000
0.0
0.5
1.0
1.5
2.0

(a)

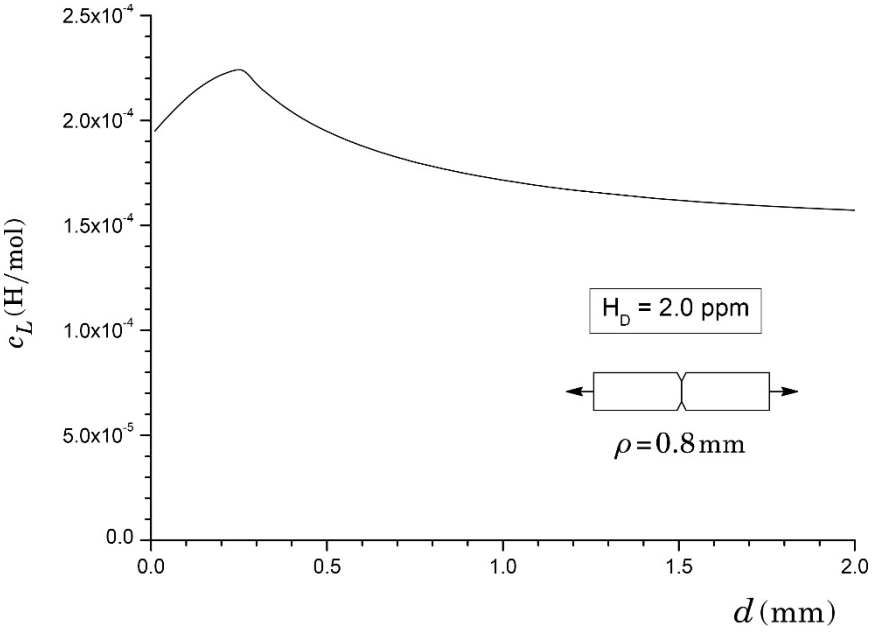
H_D = 2.0 ppm
$\rho = 0.8\,\mathrm{mm}$
c_L (H/mol)
d (mm)
2.5x10^{-4}
2.0x10^{-4}
1.5x10^{-4}
1.0x10^{-4}
5.0x10^{-5}
0.0
0.0
0.5
1.0
1.5
2.0

(b)

Figure 11

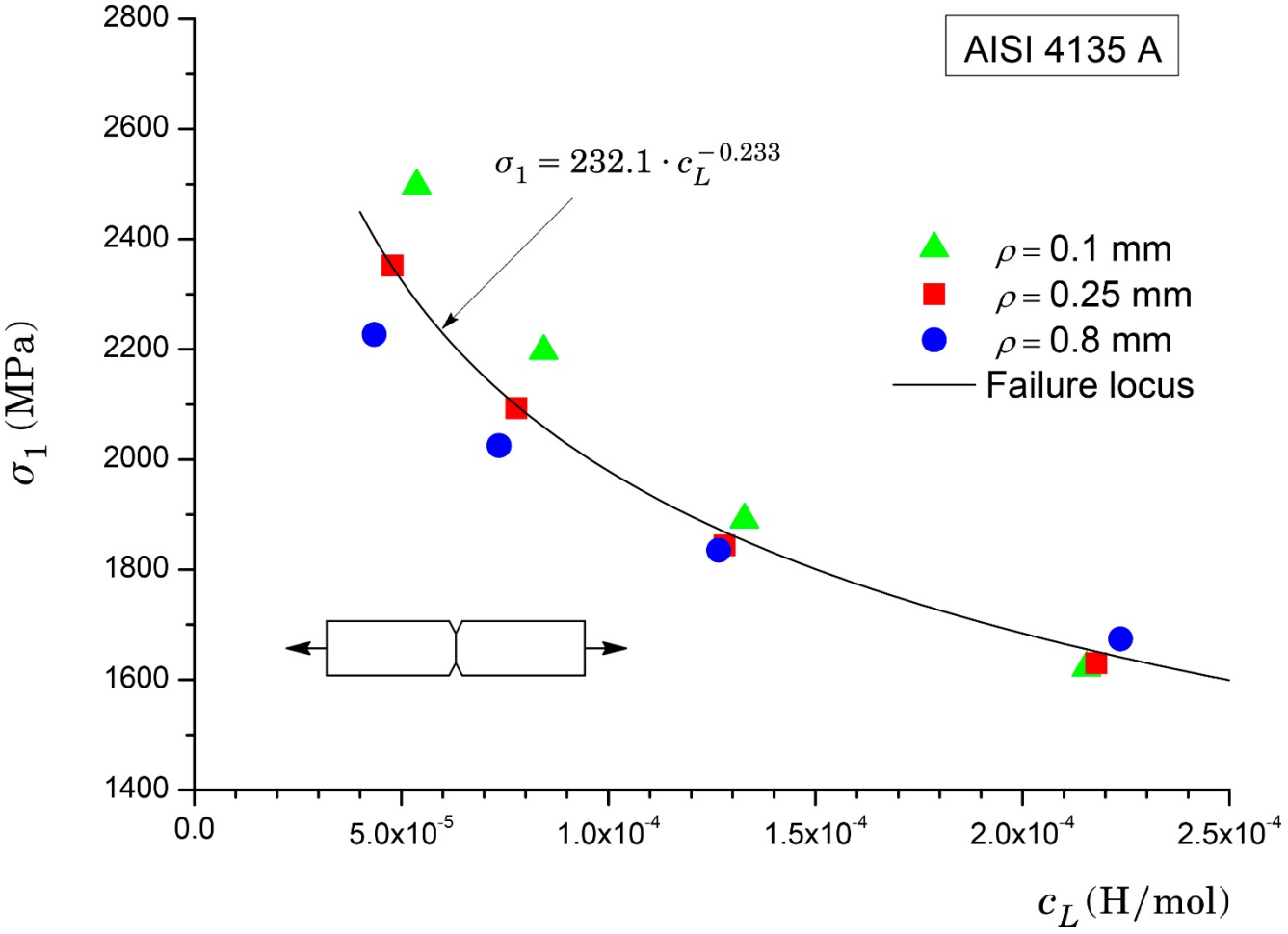
AISI 4135 A
$\sigma_1 = 232.1 \cdot c_L^{-0.233}$
$\rho = 0.1$ mm
$\rho = 0.25$ mm
$\rho = 0.8$ mm
Failure locus
σ_1 (MPa)
c_L (H/mol)
2800
2600
2400
2200
2000
1800
1600
1400
0.0
5.0x10^{-5}
1.0x10^{-4}
1.5x10^{-4}
2.0x10^{-4}
2.5x10^{-4}

Figure 12

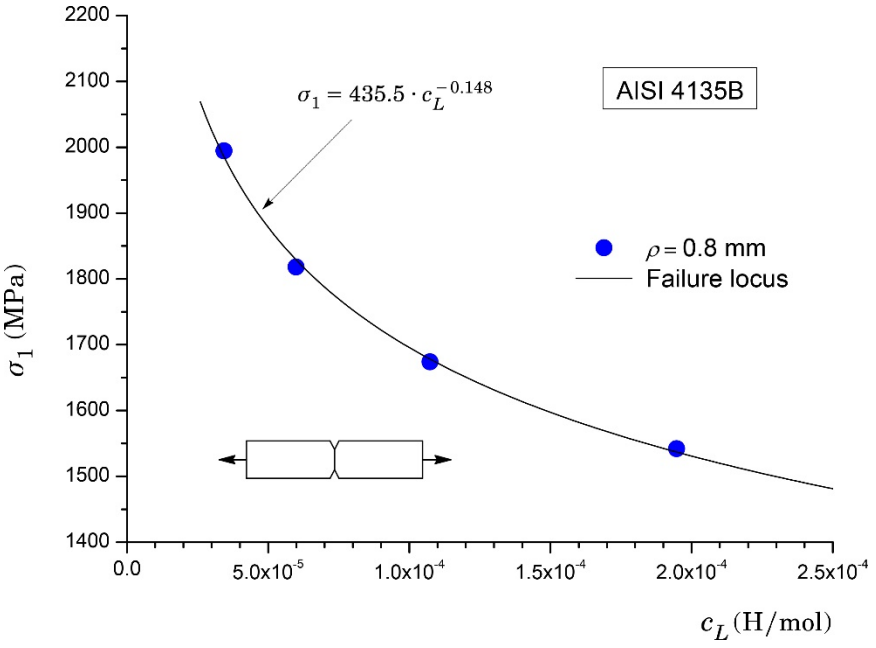
$\sigma_1 = 435.5 \cdot c_L^{-0.148}$
AISI 4135B
ρ = 0.8 mm
Failure locus
σ_1 (MPa)
c_L (H/mol)
2200
2100
2000
1900
1800
1700
1600
1500
1400
0.0
5.0x10^{-5}
1.0x10^{-4}
1.5x10^{-4}
2.0x10^{-4}
2.5x10^{-4}

(a)

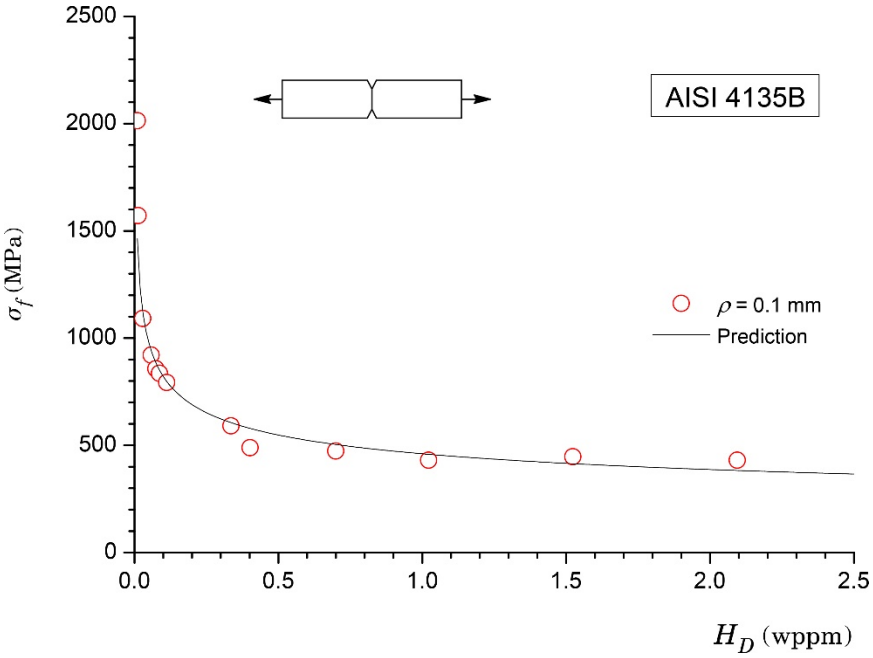
AISI 4135B
ρ = 0.1 mm
Prediction
σ_f (MPa)
H_D (wppm)
2500
2000
1500
1000
500
0
0.0
0.5
1.0
1.5
2.0
2.5

(b)

Figure 13

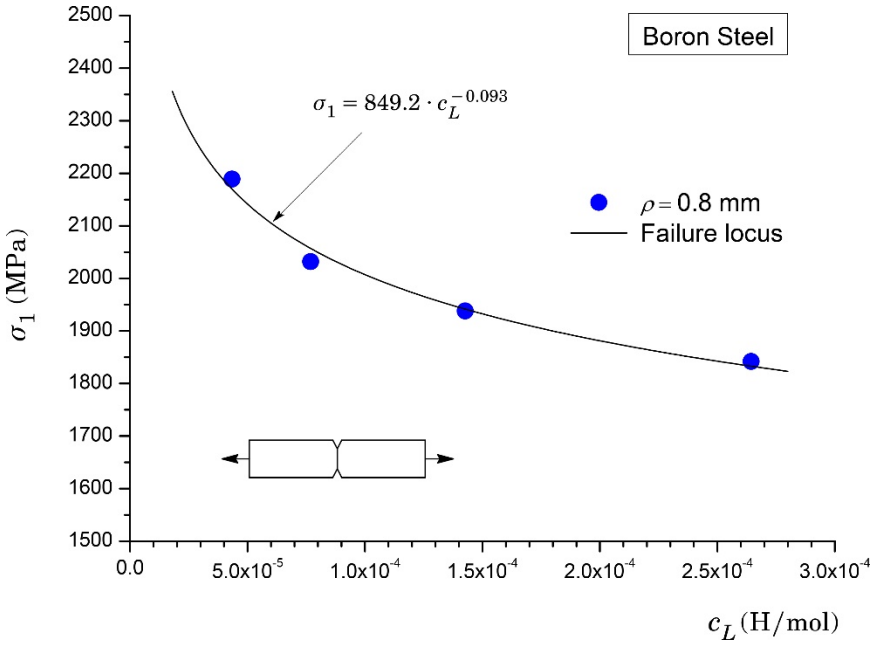
Boron Steel
$\sigma_1 = 849.2 \cdot c_L^{-0.093}$
ρ = 0.8 mm
Failure locus
σ_1 (MPa)
c_L (H/mol)
2500
2400
2300
2200
2100
2000
1900
1800
1700
1600
1500
0.0
5.0x10^{-5}
1.0x10^{-4}
1.5x10^{-4}
2.0x10^{-4}
2.5x10^{-4}
3.0x10^{-4}

(a)

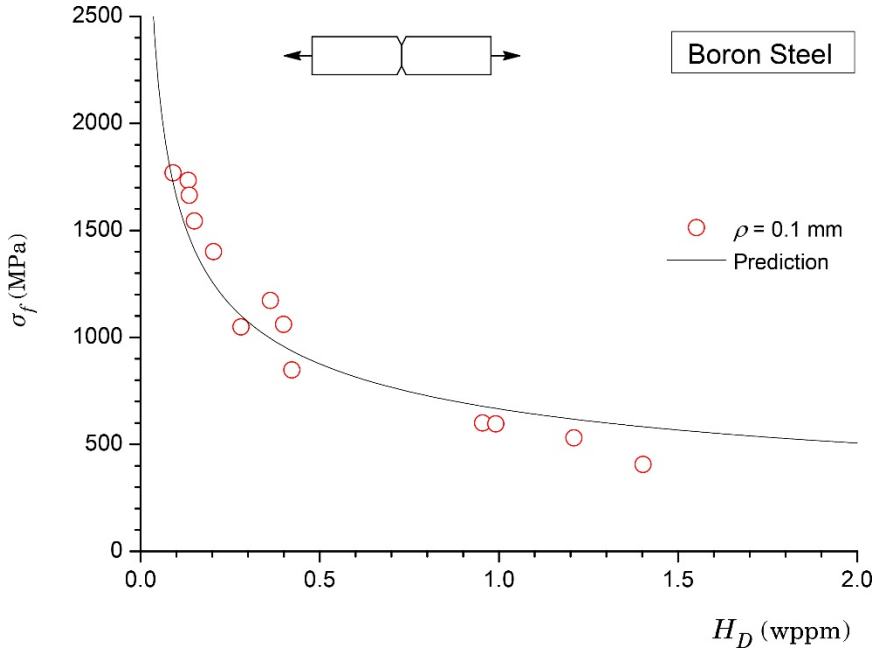
Boron Steel
ρ = 0.1 mm
Prediction
σ_f (MPa)
H_D (wppm)
2500
2000
1500
1000
500
0
0.0
0.5
1.0
1.5
2.0

(b)

Figure 14